LETTER

Dynamically encircling an exceptional point for asymmetric mode switching

Jörg Doppler[1], Alexei A. Mailybaev[2], Julian Böhm[3], Ulrich Kuhl[3], Adrian Girschik[1], Florian Libisch[1], Thomas J. Milburn[4], Peter Rabl[4], Nimrod Moiseyev[5] & Stefan Rotter[1]

Physical systems with loss or gain have resonant modes that decay or grow exponentially with time. Whenever two such modes coalesce both in their resonant frequency and their rate of decay or growth, an 'exceptional point' occurs, giving rise to fascinating phenomena that defy our physical intuition[1–6]. Particularly intriguing behaviour is predicted to appear when an exceptional point is encircled sufficiently slowly[7,8], such as a state-flip or the accumulation of a geometric phase[9,10]. The topological structure of exceptional points has been experimentally explored[11–13], but a full dynamical encircling of such a point and the associated breakdown of adiabaticity[14–21] have remained out of reach of measurement. Here we demonstrate that a dynamical encircling of an exceptional point is analogous to the scattering through a two-mode waveguide with suitably designed boundaries and losses. We present experimental results from a corresponding waveguide structure that steers incoming waves around an exceptional point during the transmission process. In this way, mode transitions are induced that transform this device into a robust and asymmetric switch between different waveguide modes. This work will enable the exploration of exceptional point physics in system control and state transfer schemes at the crossroads between fundamental research and practical applications.

Exceptional points (EPs), also called non-Hermitian degeneracies or branch points, have turned out to be at the origin of many counter-intuitive phenomena appearing in physical systems that experience gain or loss[1–6]. Such external influences on a system require a non-Hermitian description that incorporates non-conservation of energy resulting from an external input or output. Rather than being merely a perturbative correction, gain and loss can entirely turn the behaviour of a system upside down when approaching an EP. Consider here, for example, the recent demonstrations of unidirectional invisibility[22–24], loss-induced suppression and revival of lasing[25–27], and single-mode lasers with gain and loss[28,29] or directional output[30], all of which were realized at or close to an EP. These studies already nicely demonstrate the potential of EPs for novel effects and devices, but the full capability of EPs can be accessed when the EP is not just approached or swept across, but dynamically encircled[7,8].

Originally, it was believed that a slow encircling of an EP would result in an adiabatic evolution of states and a corresponding state flip[9], but more recent work has rigorously shown that the same non-Hermitian components necessary for the observation of an EP actually prevent an application of the adiabatic theorem[14–21]. Instead, non-adiabatic transitions lead to a chiral behaviour, in the sense that encircling an EP in a clockwise or a counter-clockwise direction results in different final states[14,18,21]. While this fascinating feature has great potential for quantum control and switching protocols, it has so far defied any experimental realization. This is because to observe the non-adiabatic contributions requires a fully dynamical encircling of the EP that goes beyond the quasi-static experiments reported so far[11–13]. A dynamically

resolved experiment is, however, extremely challenging, because of the precise control required of the two exponentially amplified or damped resonant modes that meet at the EP, which must also be decoupled from all other modes present in a system.

Proposals to overcome this problem have meanwhile been put forward, such as to map the dynamical encircling of an EP to the polarization evolution in a stratified non-transparent medium[15], but the implementation requirements involved prevented an experimental realization for this case too. Here, we overcome such difficulties by demonstrating that waveguides with two transverse modes can be suitably engineered such that the transmission through them is equivalent to a slow dynamical encircling of an EP. In this way we make the recently discussed dynamical features of EPs directly accessible through established waveguide technology as used for the transmission of sound, light, microwaves and matter waves.

An EP arises when an open system described by the Schrödinger-type equation $i\partial_t \psi = H\psi$ features two resonant modes that coalesce. Such a scenario can conveniently be captured by the following non-Hermitian 2×2 Hamiltonian:

$$H = \begin{pmatrix} \delta - i\gamma_1/2 & g \\ g & -i\gamma_2/2 \end{pmatrix} \qquad (1)$$

where g denotes the coupling and δ the detuning; γ_1 and γ_2 are the respective loss rates of the two relevant modes. At the specific parameter configuration $\delta_{EP} = 0$ and $g_{EP} = |\gamma_1 - \gamma_2|/4$, both the eigenvalues and eigenvectors of this Hamiltonian coalesce, which is the hallmark of the EP. As shown in Fig. 1, the vicinity of this point exhibits a characteristic structure of a self-intersecting Riemann surface. The EP marks the branch point (at the centre of each panel in Fig. 1a, b) at which the Riemann surface splits. It is this topological structure that allows one to encircle the EP such that the two eigenmodes interchange: for such a state-flip two system parameters need to be continuously changed in time t (for example, the coupling $g = g(t)$ and the detuning $\delta = \delta(t)$) along a closed loop in parameter space around the EP. This system evolution is described by the now time-dependent Hamiltonian (1) in the corresponding Schrödinger-type equation $i\partial_t \psi(t) = H(t)\psi(t)$. If the system dynamics is fully adiabatic, a flip between the two states is realized upon encircling the EP such that the lower state becomes the upper one (Fig. 1a, left). As was found only recently[14], however, contributions due to the breakdown of adiabaticity in non-Hermitian systems always enter dominantly whenever both encircling directions are considered. In the case above, traversing the same parameter loop in the opposite direction thus leads to the situation that the lower state returns to itself rather than to the upper state (Fig. 1b, left). This enforces an overall asymmetric behaviour such that the state that is selected at the end of a loop depends only on the loop's encircling direction, but not on its starting point—compare Fig. 1a and Fig. 1b for a
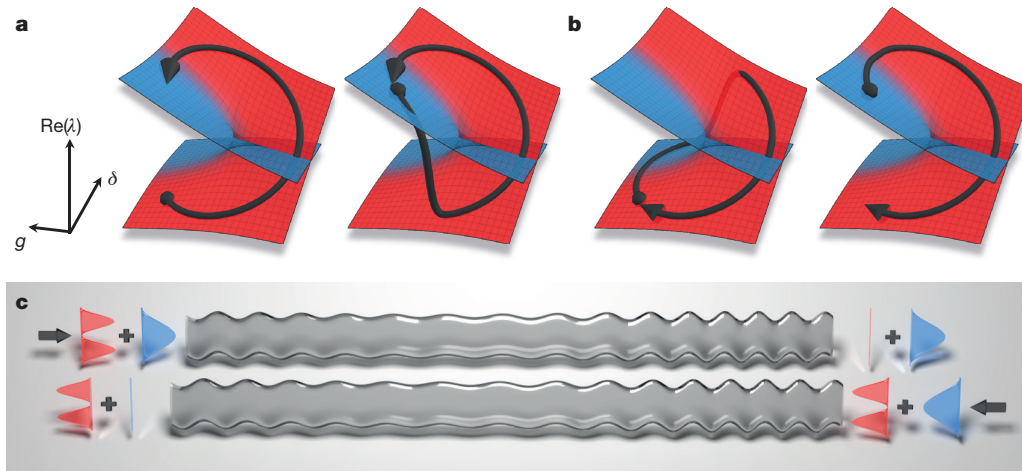
Figure 1 | Mode evolution in the vicinity of an exceptional point. To demonstrate the non-adiabatic nature of dynamically encircling an EP degeneracy, we show trajectories with different encircling directions, starting on both of the Riemann sheets involved (shown as red and blue surfaces). The results for the state evolution of the Schrödinger-type equation $i\partial_x\psi(x) = H(x)\psi(x)$, projected onto their respective Riemann sheets, are shown as black lines: the larger the contribution of an eigenvector, the closer it follows the corresponding eigensheet[21]. **a**, Dynamics of two states with starting points on different sheets during a counter-clockwise loop around the EP (as seen from the top). **b**, Same as **a** for a clockwise loop. In both **a** and **b** the end points of the loops depend only on the encircling direction, not on their starting point. **c**, Schematic of an asymmetric mode-switch that projects the above EP-encircling to a waveguide that strongly attenuates one of its two transverse modes, depending on the injection direction. The parameter-space trajectories describing counter-clockwise and clockwise loops around the EP shown in **a** and **b** correspond to the left and right injection, respectively.

counter-clockwise and clockwise encircling, respectively. On a very fundamental level, these features are connected with the Stokes phenomenon of asymptotics[15,16] as well as with the theory of singular perturbations and stability loss delay[21]—concepts that can be used to determine whether and when the non-adiabatic excursions shown in Fig. 1a, b occur, as well as to estimate their latest possible onset time[21].

To observe this behaviour in a realistic environment, we now map the Hamiltonian in equation (1) onto the problem of microwave transmission through a smoothly deformed metallic waveguide in the presence of absorption (see Fig. 1c). The waveguide is extended along the x axis and we restrict the following discussion to a single transverse dimension y. Within this framework, the parametrical encircling of the EP from the 2×2 model shown above translates to a slow variation of a periodic boundary modulation along the waveguide. Directly at the EP, both the Bloch wavenumbers K and the Bloch modes Λ of the electric field distribution $\phi(x,y) = \Lambda(x,y)e^{iKx}$ coalesce. More specifically, the harmonic solutions $\varphi(x,y,t) = \phi(x,y)e^{-i\omega t}$ for fields oscillating with frequency ω obey the Helmholtz equation:

$$\Delta\phi(x,y) + V(x,y)\phi(x,y) = 0 \qquad (2)$$

where Δ is the Laplace operator in two dimensions, $V(x,y) = \varepsilon(x,y)\omega^2/c^2$ is a complex potential proportional to the dielectric function ε, and c is the speed of light. For a straight rectangular waveguide with a fixed width W in the y direction the solutions of equation (2) in the absence of losses are $\phi_n(x,y) = u_n(y)e^{ik_n x}$ with transverse mode functions $u_n(y) = \sin(n\pi y/W)$ and wavevectors $k_n = \sqrt{\omega^2/c^2 - n^2\pi^2/W^2}$. By choosing an appropriate input frequency ω, the transmission problem can naturally be reduced to only two propagating modes $n = 1, 2$. To implement a controlled coupling between these modes, we consider a waveguide subject to a boundary modulation $\xi(x) = \sigma\sin(k_b x)$, as shown in Fig. 1c. By choosing the boundary wavenumber $k_b = k_1 - k_2 + \delta$, where $|\delta| \ll k_b$, near-resonant scattering between the otherwise very different modes ϕ_1 and ϕ_2 occurs. The full solution for the propagating field can be written in the form:

$$\phi(x,y) = \alpha_1(x)\phi_1(x,y) + \alpha_2(x)\phi_2(x,y) \qquad (3)$$

Employing a Floquet–Bloch ansatz, we obtain a Schrödinger-type equation for the slowly varying modal amplitudes $\psi(x) = (c_1(x), c_2(x))^T = e^{-i\delta x}(\sqrt{ik_1}\,\alpha_1(x), \sqrt{-ik_2}\,\alpha_2(x))^T$:

$$i\partial_x\begin{pmatrix} c_1(x) \\ c_2(x) \end{pmatrix} = \begin{pmatrix} \delta(x) - i\gamma_1/2 & g(x) \\ g(x) & -i\gamma_2/2 \end{pmatrix}\begin{pmatrix} c_1(x) \\ c_2(x) \end{pmatrix} \qquad (4)$$

(See Supplementary Information for a more detailed derivation verified by numerical simulations.) The slow variation of $\delta = \delta(x)$ and $g = g(x) \propto \sigma(x)$ in Hamiltonian (1) is then directly implemented in the waveguide through a smooth variation of the modulation potential $V(x,y)$, which leaves the validity of equations (3) and (4) intact. Finally, owing to the even and odd symmetry of $u_1(y)$ and $u_2(y)$, an absorbing material placed close to the centre of the waveguide gives rise to losses $\gamma_1 \gg \gamma_2$. With the above, all parameters in the non-Hermitian Hamiltonian H in equation (1) are determined. However, instead of governing the temporal dynamics (in time), H determines here the mode propagation in the longitudinal direction x. Correspondingly, the requirement of encircling the EP slowly (in time t) is transferred here to a slow variation of the boundary parameters along the propagation direction x (see Fig. 1c). Quite remarkably, a right and left injection into the waveguide corresponds to a clockwise and counter-clockwise encircling direction of the EP, respectively, yielding a specific and different output mode depending only on the side from which the waves are injected.

First numerical results following this procedure are shown in Fig. 2, where we rely on a parametrization of the waveguide modulation envelope, $\sigma(x) = (\sigma_0/2)(1 - \cos(2\pi x/L))$ that is restricted to a finite region ($x \in [0, L]$) and perfectly connects to flat semi-infinite waveguides outside this domain. Deviating from what is shown in Fig. 1, we also choose the detuning δ to be linear in x, $\delta(x) = \delta_0(2x/L - 1) + \rho$, which, together with $\sigma(x)$ from above, still describes a loop around the EP, since the endpoints of this parameter-trajectory correspond to identical waveguide configurations (see Supplementary Information for details). By implementing these design considerations in a waveguide first with uniform (bulk) loss in the transverse direction, the desired asymmetric switching of modes is, indeed, fully realized, as follows. Either mode entering from the left (Fig. 2a, b) is scattered into the first mode at the right exit lead. In contrast, any mode injected from the right side of the waveguide yields the second mode at the left exit lead (Fig. 2c, d). On the downside, however, the large overall loss both states have to acquire in order to manifest this asymmetry considerably deteriorates the quality of this switching mechanism. Additionally, the requirement of slow
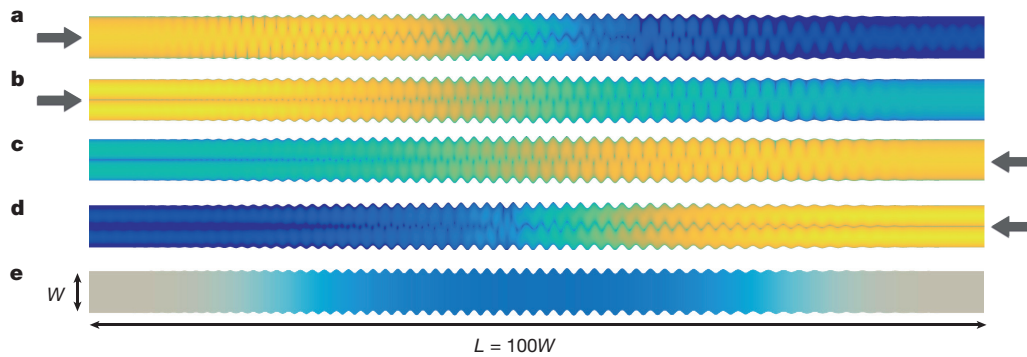
Figure 2 | Chiral transport in the presence of bulk absorption.
a–**d**, Numerically simulated modal wavefunction intensities for a waveguide with a length-to-width ratio of $L/W = 100$ (the depicted dimensions are not to scale). Shown are results for different input modes and injection directions: arrows indicate the side from which the waveguide is excited; the first mode is injected in **a** and **c**, and the second mode is injected in **b** and **d**. We use a logarithmic scale for the respective intensities since the overall dissipation is very strong, as is evident from

the corresponding values for transmission T_{nm} from mode n into mode m: $T_{11} = 2.5 \times 10^{-11}$, $T_{21} = 8.9 \times 10^{-7}$, $T_{12} = 7.0 \times 10^{-14}$ and $T_{22} = 8.4 \times 10^{-12}$. The normalized mode profiles at the waveguide exit, which clearly show the efficient mode-switching, are shown in Supplementary Fig. 10. **e**, Plot of the absorption strength, which is gradually switched on and off, but is uniform in the transverse direction. Specifically, for the above waveguide, $\omega W/c\pi = 2.05$, $\sigma_0/W = 0.07$, $\delta_0 W = 0.5$ and $\rho W = -0.5$.

encircling translates into a long and bulky device with many boundary oscillations.

To overcome both of these obstacles, we devised the following two strategies. First, we designed the absorption in the waveguide to follow a spatial pattern that minimizes (maximizes) the dissipation for the mode featuring the adiabatic (non-adiabatic) transition, while leaving the topology of the loop around the EP intact (see Supplementary Information for details). Remarkably, no matter which spatial profile we choose for the absorber, the reciprocity principle ensures that our design works for both transmission directions equivalently. Second, we employed a combination of quasi-Newton methods with stochastic algorithms to decrease the system length, resulting in a length-to-width ratio reduced by a factor of four as compared to the devices shown in Fig. 2. In this optimization, we tuned the parameters σ_0, δ_0 and ρ such as to reduce the waveguide length while making sure that the resulting device still maintains the frequency robustness inherent in our design

principle (see Supplementary Fig. 11 for this efficient device geometry and the corresponding numerical results).

To demonstrate its potential for real-world applications, we provide here the first experimental realization of the above protocol, implemented in a surface-modulated microwave setup following the proposed efficient design (Fig. 3a, b). Measuring the modal transmission intensities T_{nm} from mode n into mode m as a function of the input signal frequency, we unambiguously confirm the asymmetric switching effect (see Fig. 3c): An arbitrary combination of modes injected from the left side of the waveguide is transmitted into the first mode when arriving at the exit lead on the right (T_{11} and T_{21} dominate the transmission of the first and second mode, respectively, with transmission intensity ratios $T_{11}/T_{12} = 20.6$ and $T_{21}/T_{22} = 23.0$). At the same time, the second mode is produced on the left for injection from the right (T'_{12} and T'_{22} dominate the respective modal transmission, where the primed quantities are those for
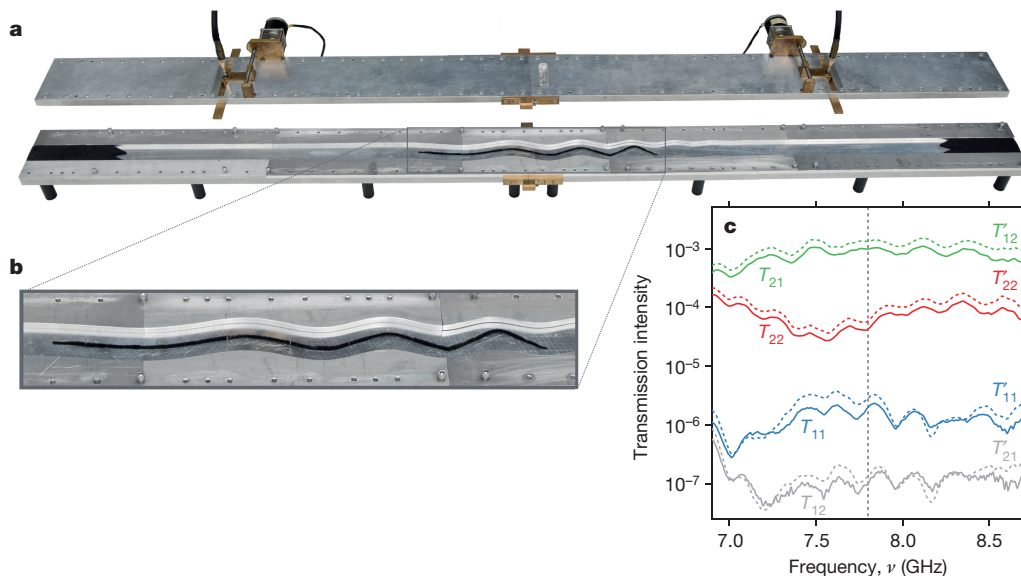

Figure 3 | Microwave measurements. a, Photograph of the optimized waveguide channel used in the experiment, with a surface-modulated region of length $L = 1.25$ m and width $W = 5$ cm (image credit J.B. and U.K., 2015). Within this setup, input and output antennas are placed 1.5 m apart (shown on the top plate). Black foam is used both as an absorber in the centre of the waveguide (magnified in **b**) and to mitigate the reflection into the entrance and exit leads. The setup is engineered for

a target frequency of $\nu = 7.8$ GHz (shown by a dashed vertical line in **c**), but the design ensures applicability over a broad frequency interval. **c**, Measured frequency-dependent transmission intensities T_{nm} (T'_{nm}) from mode n into mode m for injection from the left (right) are shown by solid (dashed) lines. The waveguide parameters here are $\omega W/c\pi = 2.6$, $\sigma_0/W = 0.16$, $\delta_0 W = 1.25$ and $\rho W = -1.8$.

injection from the right, with ratios $T'_{12}/T'_{11} = 463.4 \approx T_{21}/T_{11} = 488.6$ and $T'_{22}/T'_{21} = 425.9 \approx T_{22}/T_{12} = 438.4$). Note that the slight violation of the reciprocity property $T'_{nm} = T_{mn}$ observed in the experiment (see Fig. 3c) is due to the magnetized absorber material (see details in Methods), which is needed to obtain a sufficiently strong absorption in the corresponding frequency range (without the absorber, the experiment is fully reciprocal). This small non-reciprocity is, however, not essential for the operation of our device, since the respective intensity ratios are approximately the same for both injection directions. Most importantly, the experimental data proves the very strong robustness of these transmission values with respect to variations of the input frequency—a broad-band feature that is a direct consequence of our design principle, which ensures operability also in the presence of small variations of the waveguide parameters. The shortened device for which the length-to-width ratio is now $L/W = 25$ also vastly outperforms the longer device in Fig. 2 (for which $L/W = 100$), not only in terms of length-to-width ratio, but also in terms of the output intensity which is here increased by six orders of magnitude.

As an ultimate proof that the functionality of our device hinges on a dynamical EP-encircling, we also fabricated five waveguides, with individual boundary frequencies and amplitudes distributed over the parameter loop around the EP inherent in the chirped waveguide design of Fig. 3. Concatenating these stroboscopic results allows us to eliminate the dynamics in the loop around the EP, resulting in a parametric EP-encircling for which all non-adiabatic contributions should vanish. Remarkably, our results for this case (see Supplementary Fig. 9) fully reproduce the symmetric state flips that were observed in all previous experiments[11–13] where such a parametric EP-encircling was implemented.

In summary, our work constitutes the first experimental encircling of an exceptional point that stays faithful to the full dynamical and non-adiabatic behaviour occurring in this context. In this way, we have devised a notably platform-independent approach to mode switching that is implementable not just for microwaves, but readily applicable also to light, acoustic or matter waves. An accompanying paper also reports on a dynamical EP-encircling in an optomechanical setup[31].

1.   Berry, M. V. Physics of nonhermitian degeneracies. *Czech. J. Phys.* **54**, 1039–1047 (2004).
2.   Bender, C. M. Making sense of non-Hermitian Hamiltonians. *Rep. Prog. Phys.* **70**, 947 (2007).
3.   Rotter, I. A non-Hermitian Hamilton operator and the physics of open quantum systems. *J. Phys. A* **42**, 153001 (2009).
4.   Moiseyev, N. *Non-Hermitian Quantum Mechanics* (Cambridge Univ. Press, 2011).
5.   Heiss, W. D. The physics of exceptional points. *J. Phys. A* **45**, 444016 (2012).
6.   Cao, H. & Wiersig, J. Dielectric microcavities: model systems for wave chaos and non-Hermitian physics. *Rev. Mod. Phys.* **87**, 61–111 (2015).
7.   Lefebvre, R., Atabek, O., Šindelka, M. & Moiseyev, N. Resonance coalescence in molecular photodissociation. *Phys. Rev. Lett.* **103**, 123003 (2009).
8.   Atabek, O. *et al.* Proposal for a laser control of vibrational cooling in Na₂ using resonance coalescence. *Phys. Rev. Lett.* **106**, 173002 (2011).
9.   Latinne, O. *et al.* Laser-induced degeneracies involving autoionizing states in complex atoms. *Phys. Rev. Lett.* **74**, 46–49 (1995).
10. Mailybaev, A. A., Kirillov, O. N. & Seyranian, A. P. Geometric phase around exceptional points. *Phys. Rev. A* **72**, 014104 (2005).
11. Dembowski, C. *et al.* Experimental observation of the topological structure of exceptional points. *Phys. Rev. Lett.* **86**, 787–790 (2001).
12. Lee, S.-B. *et al.* Observation of an exceptional point in a chaotic optical microcavity. *Phys. Rev. Lett.* **103**, 134101 (2009).
13. Gao, T. *et al.* Observation of non-Hermitian degeneracies in a chaotic exciton-polariton billiard. *Nature* **526**, 554–558 (2015).
14. Uzdin, R., Mailybaev, A. & Moiseyev, N. On the observability and asymmetry of adiabatic state flips generated by exceptional points. *J. Phys. A* **44**, 435302 (2011).
15. Berry, M. V. Optical polarization evolution near a non-Hermitian degeneracy. *J. Opt.* **13**, 115701 (2011).
16. Berry, M. V. & Uzdin, R. Slow non-Hermitian cycling: exact solutions and the Stokes phenomenon. *J. Phys. A* **44**, 435303 (2011).
17. Demange, G. & Graefe, E.-M. Signatures of three coalescing eigenfunctions. *J. Phys. A* **45**, 025303 (2012).
18. Gilary, I., Mailybaev, A. A. & Moiseyev, N. Time-asymmetric quantum-state-exchange mechanism. *Phys. Rev. A* **88**, 010102 (2013).
19. Graefe, E.-M., Mailybaev, A. A. & Moiseyev, N. Breakdown of adiabatic transfer of light in waveguides in the presence of absorption. *Phys. Rev. A* **88**, 033842 (2013).
20. Kaprálová-Žďánská, P. R. & Moiseyev, N. Helium in chirped laser fields as a time-asymmetric atomic switch. *J. Chem. Phys.* **141**, 014307 (2014).
21. Milburn, T. J. *et al.* General description of quasiadiabatic dynamical phenomena near exceptional points. *Phys. Rev. A* **92**, 052124 (2015).
22. Lin, Z. *et al.* Unidirectional invisibility induced by 𝒫𝒯-symmetric periodic structures. *Phys. Rev. Lett.* **106**, 213901 (2011).
23. Regensburger, A. *et al.* Parity–time synthetic photonic lattices. *Nature* **488**, 167–171 (2012).
24. Feng, L. *et al.* Experimental demonstration of a unidirectional reflectionless parity-time metamaterial at optical frequencies. *Nat. Mater.* **12**, 108–113 (2012).
25. Liertzer, M. *et al.* Pump-induced exceptional points in lasers. *Phys. Rev. Lett.* **108**, 173901 (2012).
26. Brandstetter, M. *et al.* Reversing the pump dependence of a laser at an exceptional point. *Nat. Commun.* **5**, 4034 (2014).
27. Peng, B. *et al.* Loss-induced suppression and revival of lasing. *Science* **346**, 328–332 (2014).
28. Hodaei, H., Miri, M.-A., Heinrich, M., Christodoulides, D. N. & Khajavikhan, M. Parity-time–symmetric microring lasers. *Science* **346**, 975–978 (2014).
29. Feng, L., Wong, Z. J., Ma, R.-M., Wang, Y. & Zhang, X. Single-mode laser by parity-time symmetry breaking. *Science* **346**, 972–975 (2014).
30. Peng, B. *et al.* Chiral modes and directional lasing at exceptional points. *Proc. Natl Acad. Sci.* **113**, 6845–6850 (2016).
31. Xu, H., Mason, D., Jiang, L. & Harris, J. G. E. Topological energy transfer in an optomechanical system with exceptional points. *Nature* http://www.dx.doi.org/10.1038/nature18604 (2016).

METHODS

Numerical simulations. In our numerical simulations we solve the Helmholtz equation (2) on a finite-difference grid by means of a Green's function method[32]. The transmission (reflection) amplitudes t_{nm} (r_{nm}) are then determined by projecting the system's Green's function onto the flux-carrying modes in the semi-infinite leads that are attached to the scattering geometry. The corresponding intensities are given by $T_{nm} = |t_{nm}|^2$ and $R_{nm} = |r_{nm}|^2$, respectively. We choose the real part of the potential $V(x, y)$ to be finite (infinite) inside (outside) the cavity, corresponding to Dirichlet boundary conditions, and the imaginary part of the potential is determined such as to satisfy the protocol described in the main text.

Experimental setup. The experimental device is an aluminium waveguide with dimensions $L \times W \times H = 2.38\,\text{m} \times 5\,\text{cm} \times 8\,\text{mm}$. Figure 3a shows the surface modulation that steers the modes around the EP. Our microwave experiment allows us to define the corresponding boundary conditions very accurately and to place the magnetized absorbing foam material (LS-10211 foam from ARC Technologies, $W \times H = 2.5\,\text{mm} \times 5\,\text{mm}$) with sub-wavelength ($<0.5\,\text{mm}$) precision. Additional absorbers (LS-14 and LS-16 foams from Emerson and Cuming, $W \times L = 5\,\text{cm} \times 17.5\,\text{cm}$) are employed to mimic semi-infinite leads.

Microwave measurements. To probe the sinusoidal modes formed by the z component of the electric field E_z (ref. 33), we use two microwave antennas 1.5 m apart. The antennas are fixed onto motor-controlled, moveable slides and measure the complex transmission signal outside of the modulated surface area at 2×2 points along the y axis of the antennas. For the measurements we employ microwaves with a frequency around $\nu = 7.8\,\text{GHz}$, which is well below the cutoff frequency for TE$_0$ modes ($\nu_c = c/2H = 18.75\,\text{GHz}$), such that only the first two sinusoidal TE$_0$ modes contribute to the transport. By applying the twofold sine transformation:

$$t_{nm} = \frac{1}{2} \sum_{y_1 y_2} t'(y_1, y_2) \sin\left(\frac{n\pi}{W} y_1\right) \sin\left(\frac{m\pi}{W} y_2\right)$$

where $t'(y_1, y_2)$ denotes the normalized transmission measured between antenna 1 at position y_1 and antenna 2 at position y_2, we obtain the transmission matrix t_{nm} in its mode representation. The normalization is necessary to overcome the frequency dependent coupling of the two antennas, and is given by:

$$t'(y_1, y_2) = \frac{t(y_1, y_2)}{\sqrt{(1 - |\langle r_1^a \rangle|^2)(1 - |\langle r_2^a \rangle|^2)}}$$

Here, $t(y_1, y_2)$ describes the transmission amplitude and $\langle r_1^a \rangle$ ($\langle r_2^a \rangle$) denotes the measured reflection amplitude at antenna 1 (antenna 2), averaged over all positions y_1 (y_2) and over a frequency window of 0.076 GHz. The measured reflection amplitudes are dominated by an imperfect impedance matching between the antenna and the channel. This results in a strong reflection signal originating from the antenna itself, which contains no information about the waveguide. We thus normalize the intensity fed into the system with the denominator in the above expression for $t'(y_1, y_2)$, which allows us to compare the transmission in a broader frequency range.

32. Libisch, F., Rotter, S. & Burgdörfer, J. Coherent transport through graphene nanoribbons in the presence of edge disorder. *New J. Phys.* **14**, 123006 (2012).
33. Dietz, O., Kuhl, U., Stöckmann, H.-J., Makarov, N. M. & Izrailev, F. M. Microwave realization of quasi-one-dimensional systems with correlated disorder. *Phys. Rev. B* **83**, 134203 (2011).